Applied Surface Science 496 (2019) 143610

Contents lists available at ScienceDirect

Applied Surface Science

journal homepage: www.elsevier.com/locate/apsusc

Full length article

Moisture proof hole transport layers based on CISe quantum dots for highly stable and large active area perovskite solar cells

Jae-Yup Kim[a,1], Woonhyuk Baek[b,c,1], Soyoung Kim[d], Gumin Kang[e], Il Ki Han[e], Taeghwan Hyeon[b,c,*], Minwoo Park[d,*]

[a] Department of Chemical Engineering, Dankook University, Yongin 16890, Republic of Korea
[b] School of Chemical and Biological Engineering, and Institute of Chemical Processes, Seoul National University, Seoul 08826, Republic of Korea
[c] Center for Nanoparticle Research, Institute of Basic Science (IBS), Seoul 08826, Republic of Korea
[d] Department of Chemical and Biological Engineering, Sookmyung Women's University, Seoul 04310, Republic of Korea
[e] Nanophotonics Center, Korea Institute of Science and Technology (KIST), Seoul 02792, Republic of Korea

ARTICLE INFO

Keywords:
Perovskite solar cells
CISe
Quantum dots
Stability
Organic ligands
Active area

ABSTRACT

Extensive studies have been performed to improve the environmental stability of perovskite solar cells (PSCs) with the use of inorganic charge transport layers (CTLs). However, for *n*-i-*p* structures, it is difficult to deposit *p*-type inorganic nanocrystals onto perovskites to form the CTLs because they are usually prepared in polar solvents. In this regard, hydrophobic nanoparticles dispersed in nonpolar solvents would be beneficial for their deposition onto the perovskites, thus leading to the formation of a hole transport layer (HTL). In this work, we report on the preparation of monodispersed $CuIn_{1.5}Se_3$ (CISe) quantum dots (QDs) (diameter = 4 nm) for the design of PSCs based on all-inorganic CTLs. By means of efficient hole injection and transfer process through the CISe-HTLs, impressive power conversion efficiencies (PCEs) of 13.72% and 12.19% for active areas of 0.12 cm^2 and 1.0 cm^2 are achieved, respectively, and the devices exhibit hysteresis-less behaviors. Furthermore, the devices show excellent PCE retentions of 89.2% and 74.9% after 30 d relative to their initial values at relative humidity of 25% and 50%, respectively. The hydrophobic QDs effectively suppress the penetration of moisture such that the device maintains its stability in humid environments.

1. Introduction

Perovskite solar cells (PSCs) have been considered as a promising energy supplier and an alternative to conventional solar cells [1–3]. Their power conversion efficiencies (PCE) have increased to 23.7% via the interface and compositional engineering of perovskites, and have become comparable to the values of polycrystalline silicon solar cells [4–8]. Furthermore, perovskites fabricated using low-temperature solution processes exhibit high feasibility in diverse optoelectronic devices, including field-effect transistors, light-emitting diodes, photodetectors, and memory devices, owing to their excellent charge carrier mobility and light absorption coefficients [9–18]. However, environmental stability issues in PSCs have continued to increase owing to the poor intrinsic stability of perovskites and organic charge transport layers (CTLs) [19–23].

Additives in organic CTLs comprising metal salts and electrolytes increase the hydrophilicity and severely degrade perovskites [24,25]. Even though the application of molecular engineering of organic semiconductors has been proposed to improve their stabilities, it cannot be an ultimate solution since the molecules are degraded eventually [26,27]. In this regard, dopant-free organic CTLs are more desirable for maintaining the stability of the device, but they have rarely yielded PCEs that are comparable to those of devices that employ Li- and Co-doped organic CTLs [28–30]. Furthermore, encapsulation of devices with a photocurable polymer has been considered as an effective method to preserve all the layers [31]. However, the encapsulation film is vulnerable to mechanical damages, thus allowing moisture and reactive species to easily infiltrate within the devices [32]. Additionally, residual moisture within the encapsulated devices eventually degrades the perovskite and organic CTLs [33]. Therefore, these devices require the use of inorganic CTLs to improve their intrinsic stabilities and prolong the lifetimes.

Metal oxides are an essential constituent material for CTLs, which leads to an excellent device performance and stability. Additionally, the

* Corresponding authors.
E-mail addresses: thyeon@snu.ac.kr (T. Hyeon), mwpark@sm.ac.kr (M. Park).
[1] These authors contributed equally to this work.

https://doi.org/10.1016/j.apsusc.2019.143610
Received 27 May 2019; Received in revised form 22 July 2019; Accepted 6 August 2019
Available online 07 August 2019
0169-4332/

thin, nanocrystalline, and pinhole-free metal oxide films efficiently transfer charge carriers, and protect the perovskite from moisture. The metal oxide-based CTLs are typically prepared using solution deposition protocols, such as spin coating and printing techniques [34–43]. The nanocrystals are closely packed, and are deposited on the top or bottom part with respect to the perovskite layer, thereby suppressing the penetration of moisture [34]. Nevertheless, most of the metal oxides exhibit *n*-type characteristics with the exception of a few suitable *p*-type metal oxides (CuO_x and NiO_x) used for the CTLs of PSCs [44–47]. Therefore, for the design of devices with a normal structure (*n*-i-*p*), *n*-type metal oxides have been used as electron transport layers (ETLs), while hole transport layers (HTL) have still employ *p*-type organic semiconductors, such as 2,2′,7,7′-tetrakis (*N*,*N*-di-*p*-methoxyphenylamine)-9,9′-spirobifluorene (spiro–OMeTAD) and poly(triarylamine) (PTAA). This is owing to the dissolution of the perovskite based on the coating of metal oxide nanocrystals or precursors dispersed in hydrophilic solvents. To design all inorganic CTL-based devices, inorganic nanocrystals should be dispersed in a nonpolar solvent.

As such, functionalization of inorganic nanocrystals with hydrophobic molecules can be beneficial for their homogeneous dispersion in nonpolar solvents, thus allowing their deposition onto the perovskites and the formation of the HTLs. Recently, hydrophobic HTLs comprising PbS and $CuInS_2$ (CIS) quantum dots (QDs) have been employed to improve the stability of PSCs [48–50]. The surface of CIS QDs were capped with oleylamine, which exhibited a PCE retention of 85% relative to their initial value at a humid atmosphere (relative humidity, RH = 50%) for 24 h [49]. Therefore, this result demonstrates high feasibility in improving device stability given the use of hydrophobic QDs. However, efficient hole extraction and transfer were not allowed when only the CIS–HTL was employed, thus exhibiting a low PCE of 6.57% [48]. Even though the additional deposition of spiro–OMeTAD onto the CIS–HTL led to an improved PCE of 13.8%, the PCE of the devices decreased again within a short time interval owing to the degradation of spiro-OMeTAD due to moisture [49]. Accordingly, QD–HTLs possessing high conductivity and hydrophobicity would be required to attain excellent device performance and stability characteristics without any supporting organic HTLs. Furthermore, the QD–HTLs on the perovskite should be thin and pinhole-free. These features will allow them to suppress direct contacts between the perovskite and metal electrodes, and also provide the facilitation of charge extraction and transfer by means of the minimized contact resistance between the QD layers.

Herein, we report on the development of the hydrophobic and conductive $CuIn_{1.5}Se_3$ QD–HTLs (CISe–HTLs) for the implementation of highly efficient and stable PSCs. The monodispersed CISe QDs in a nonpolar solvent have average diameters of 4 nm. The pinhole-free, smooth, and thin CISe–HTLs, are simply prepared by the spin coating of a colloidal solution of CISe. Furthermore, SnO_2 thin films are also employed as an efficient ETL. Therefore, all inorganic CTLs significantly improve the environmental stability of the devices without any encapsulation. The device has an impressive PCE of 13.72%, and shows excellent PCE retentions of 89.2% and 74.9% for 30 d relative to the initial values at RH = 25% and 50%, respectively. These are the best performing devices among all chalcogenide QD-based PSCs.

2. Experimental

2.1. Materials

CuI (99.998%), InI_3 (99.999%), PbI_2 (99.9985%), *Li*-bis(trifluoromethylsulfonyl)imide (Li–TFSI) (> 98%), SnO_2 colloidal solution (15% in H_2O), and anhydrous dimethylformamide (DMF) (99.8%), were purchased from Alfa Aesar. Anhydrous dimethylsulfoxide (DMSO) (99.9%), 4-*tert*-butyl pyridine (*t*BP) (96%), Se (99.99%), anhydrous ethylacetate (EA) (99.8%), anhydrous toluene (> 99.8%), and trioctylphosphine (TOP) (97%), were purchased from Sigma Aldrich. Oleylamine (OA, approximate C18 content 80–90%) was purchased from Acros. Methylammonium iodide (MAI) (99.98%) was purchased from GreatCell Solar, and Sprio–OMeTAD (> 99.5%) was purchased from Lumtec. The $CH_3NH_3PbI_3$ precursor solution was prepared by dissolving 461 mg of PbI_2, 159 mg of MAI, and 78 mg of DMSO in 600 mg of DMF. The spiro–OMeTAD solution was prepared by dissolving 56 mg of spiro–OMeTAD, 5.6 mg of Li–TFSI, and 28 mg of *t*BP in 1 mL of CB.

2.2. Synthesis of CISe QDs

All steps were performed using the standard Schlenk technique in an Ar atmosphere [51]. First, 0.5 mmol of CuI and 0.5 mmol of InI_3 were dissolved in 15 mL of oleylamine, followed by heating at 120 °C under vacuum for the formation of metal-amine complexes. Furthermore, oleylammonium selenocarbamate was prepared by dissolving 5 mmol of Se in 10 mL of oleylamine under bubbling of carbon monoxide (CO) gas. Subsequently, 1 mmol of oleylammonium selenocarbamate was injected into the metal-amine solution at 70 °C. The solution was heated at 180 °C for 20 min and produced CISe QDs. The ethanolic solution, which contained TOP as a nonsolvent, was injected into the colloidal solution of CISe to induce the precipitation of CISe QDs. Finally, after centrifugation of the solution at 12,000 rpm for 10 min, the resulting powder was dispersed in 10 mL of anhydrous toluene (Fig. S1, ESI†). The stabilities of the CISe–QD solutions were retained up to two weeks.

2.3. Solar cell fabrication

Etched ITO/glass (2.5 cm × 2.5 cm) substrates were rinsed for 10 min with acetone and 2-propanol (1:1 volume ratio) during ultrasonication. They were then rinsed with deionized (DI) water and dried in a N_2 atmosphere. Subsequently, they were treated with UV ozone for 20 min. The dilute SnO_2 solution with a composition of 6.5:1 (w/w) in DI water was deposited onto the ITO/glass substrates by spin coating at 3000 rpm for 30 s. After thermal annealing at 150 °C for 30 min, the perovskite was deposited onto the SnO_2-ETLs at 4000 rpm for 15 s, and 50 μl of EA was dripped on the rotating sample during the remaining 5 s. The samples were annealed immediately at 100 °C for 3 min. After cooling the samples, the CISe and spiro–OMeTAD solutions were spin coated onto the sample at 2500 rpm for 30 s. Au electrodes were deposited using a thermal evaporator with a constant rate of 0.5 Å/s.

2.4. Characterization

Ultraviolet-visible (UV–Vis) spectra of CISe–HTLs were obtained with a UV–Vis spectrometer (Scinco S–3100). The morphologies of CISe–HTLs were investigated using an atomic force microscope (AFM, Innova, Bruker). The transmission electron microscopy (TEM) images of the CISe QDs were obtained with the JEM–F200 (JEOL) microscope. X-ray diffraction (XRD) analyses were performed with an X-ray diffractometer (Rigaku Ultima IV). The atomic ratio of Cu, In, and Se, was obtained using inductively coupled plasma mass spectrometry (ICP–MS) analyses. The steady state photoluminescence (PL) spectra were obtained with a spectrometer (FLS 980). X-ray photoelectron spectroscopy (XPS) and ultraviolet photoelectron spectroscopy (UPS) analyses were performed using a scanning XPS microprobe (AXIS SUPRA, Kratos Inc.). The contact angles and interfacial tensions were measured with a contact angle analyzer (SmartDrop, FEMTOBIOMED Inc.). Time-resolved PL (TRPL) measurements were performed at the PL maxima of the perovskite (760 nm) using a time-correlated single photon counting module (TCSPC, MPD–PDM Series DET–40 photon counting detector, and a Pendulum CNT–91 frequency counter). This module was combined with a monochromator and a second-harmonic-generated 400 nm laser derived from a 800 nm Ti:Sapphire laser (Mai Tai, Spectra–Physics), and served as a detector and as an excitation source. The current–voltage (I—V) and photocurrent density-voltage

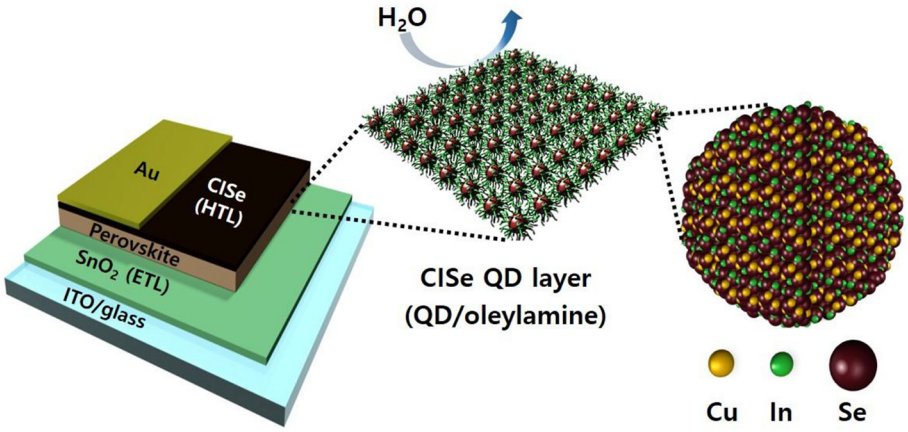

Fig. 1. Schematics of the perovskite solar cell employing a CISe–HTL. The scheme shown in higher magnification indicates that hydrophobic oleylamine ligands linked to the CISe QDs prevent moisture from infiltrating into the perovskite. The magnified single QD displays its tetragonal chalcopyrite structure.

(J–V) curves were obtained with the use of a Keithley model 2400 source meter unit. The conductivities of HTLs were measured using a four-point probe. A 300 W arc xenon lamp (Newport) in a solar simulator was used as the light source. The light intensity was adjusted to AM 1.5G with the use of an NREL-calibrated Si solar cell equipped with a KG–1 filter. The active areas of 0.12 cm^2, 0.5 cm^2, and 1.0 cm^2 were defined using metal masks. External quantum efficiency (EQE) spectra were obtained at wavelengths which ranged from 300 nm to 850 nm using IPCE equipment (PV Measurement, Inc.).

3. Results and discussion

Fig. 1 shows the schematic of the device architecture and CISe–QD model. The PSCs employing CISe–HTLs (CISe–PSCs) are composed of an indium-doped tin oxide (ITO) electrode, SnO_2–ETL, perovskite ($CH_3NH_3PbI_3$), CISe–HTL, and an Au electrode. The QD model is presented briefly in the magnified scheme, indicating a tetragonal chalcopyrite structure of CISe. Since hydrophobic OA ligands are linked to the surface of the CISe QDs, perovskite is protected from moisture and long-term stability of the devices can be achieved. As the thickness of the CISe-HTLs increases, the penetration of moisture would be more effectively suppressed. However, increasing thickness of the CISe-HTLs inhibits the charge transport due to long alkyl chains. Therefore, the thickness of the HTLs was thoroughly controlled in this study.

Fig. 2A exhibits the TEM image of monodispersed CISe QDs with an average diameter of 4 nm. The out-of-plane X-ray diffraction (XRD) analysis of the CISe–HTL indicates that the observed peaks correspond to the tetragonal chalcopyrite structure (Fig. 2B). After the spin coating of the solution onto a glass substrate, slightly transparent, dark brown and smooth thin film was formed (Fig. S2, ESI†). Fig. 2C and D show the AFM image and the corresponding height profile of the CISe–HTL. The highly flat surface does not contain aggregated QDs or small pinhole. The average surface roughness (R_a) of the film was found to be 2.91 nm, and was advantageous for the minimization of the contact resistance, even though oleylamine ligands were supposed to hinder the hole transport process from the perovskite to the Au electrodes. Furthermore, the dramatic effect of the hydrophobic CISe QDs on the water repellency was clearly demonstrated by the contact angles of the water droplets. Fig. 2E and F show photographs of water droplets on the CISe–HTL and conventional HTL composed of spiro–OMeTAD, Li–TFSI, and *t*BP (spiro–HTL). The contact angles for the CISe–HTL and spiro–HTL were found to be 102.3° and 65.8°, respectively, demonstrating that the interfacial tension at the solid–liquid interface (γ_{sl}) of the CISe–HTL is much higher than that for the spiro–HTL. The γ_{sl} values were found to be 29.3 mN m^{-1} and 14.4 mN m^{-1} for the CISe–HTL and spiro–HTL, respectively. Furthermore, the spreading parameter (S) was also calculated in accordance with the following equation,

$$S = \gamma_{sv} - (\gamma_{sl} + \gamma_{lv}) \quad (1)$$

where γ_{sv} and γ_{lv} are the interfacial tensions at the solid–vapor and liquid–vapor interfaces, respectively. This quantitative result provides the degrees of wettability of the water droplets on the CISe–HTL and spiro–HTL. The S values were found to be −73.2 mN m^{-1} and −47.1 mN m^{-1} for the CISe–HTL and spiro–HTL, respectively. The smaller S value of the CISe–HTL compared to that for the spiro–HTL suggests that the hydrophobic oleylamine ligands suppressed the contact of water molecules. In the absence of Li–TFSI and *t*BP, the contact angle of the water droplet on the spiro–HTL increased to 72° (Fig. S3, ESI†). The additives in spiro–OMeTAD decrease the contact angle of the water droplet because the spiro–OMeTAD is hygroscopic [24]. Therefore, the additives would accelerate the degradation of both the perovskite and spiro–OMeTAD, leading to the deterioration of the stability of the devices.

We characterized the atomic bonding of CISe QDs using XPS analysis. Fig. 3A shows the XPS spectrum of CISe QDs over the entire range. The spectrum was calibrated by centering the C 1 s peak at 284 eV. The magnified XPS spectra in Fig. 3B, C and D clearly exhibit the characteristic peaks corresponding to Cu 2p, In 3d, and Se 3d, respectively. The atomic ratio of our QDs was revealed using ICP–MS analyses. From the stoichiometry of the CISe QDs, it has been known that the atomic concentration of In determines their band gap (E_g) and electrical conductivity [52]. Even though a lower concentration of In (ex. Cu: In = 1:1) compared to that of the QDs slightly increases the conductivity, the E_g becomes narrow [53]. This does not result in a suitable band alignment of the CISe–HTL with the perovskite. Therefore, we controlled the atomic ratio of CISe QDs to 1:1.5:3 to broaden E_g. It has been known that the preferential coordination between Cu^{2+} and Se^{2-} induces the ionic segregation in the CISe QDs as their core and shell regions tend to be Cu-rich and In-rich, respectively [54,55]. Therefore, the smaller CISe QDs have a higher ratio of In to Cu, since In atoms are strongly driven to the surface of the QDs as their sizes are reduced. Based on our previous study, we selected the reaction temperature of 180 °C to obtain the target size, composition, and E_g of the CISe QDs [54].

The band structure of the CISe–HTLs should be suitable for perovskite to allow efficient hole injection and transfer. When the hole injection barrier becomes low, the hole injection process from the perovskite to the CISe–HTL would be greatly facilitated, simultaneously increasing the open-circuit voltage (V_{oc}) of the devices. This is because the V_{oc} can be controlled by the valence band maximum (VBM) position of the CISe–HTLs when the other energy levels are fixed [56,57]. Therefore, the optical properties and the band structure of the

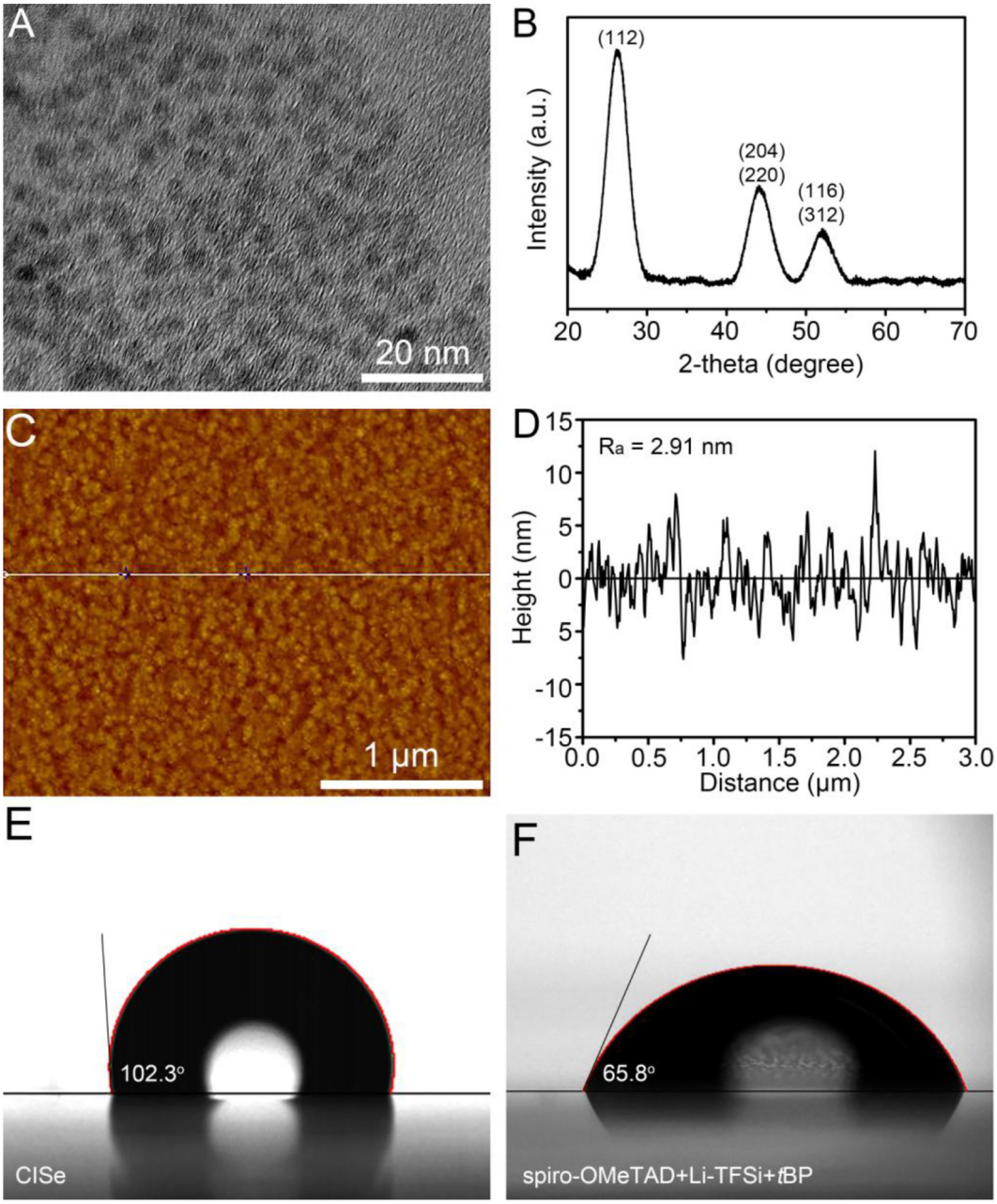

Fig. 2. (A) TEM image of as-synthesized CISe QDs. (B) Out-of-plane XRD spectrum of the CISe–HTL. (C and D) AFM image of the CISe–HTL and corresponding height profile. (E and F) Photographs indicating the respective contact angle of water droplets which contact the CISe–HTL and spiro–HTL. The measurement of contact angles was performed at room temperature and at a RH = 35%.

CISe–HTLs are of importance in the optimization of the performance of the device. Fig. 4A shows the steady state PL spectrum of the CISe–HTL. A single spectral peak was found at 944 nm, which suggests that the size of the CISe QDs is uniform. Fig. 4B shows an ultraviolet–visible (UV–Vis) spectrum of the CISe–HTL. The broad absorbance of the CISe–HTL was observed from 400 nm to 1000 nm, and the wavelength cutoff was found to be 960 nm. The E_g of the CISe–HTLs was found to be 1.3 eV from the extrapolation of the Tauc plot as depicted in the inset of Fig. 4B. The E_g of QDs strongly depends on the exciton Bohr radius (r_B). In- and Se-rich CISe QDs synthesized in this study have shown the decrease in r_B from the conventional CISe QDs (atomic ratio = 1:1:2), which leads to the increase in E_g owing to the quantum confinement effect. Therefore, the increasing E_g value from the conventional CISe QDs (1.04 eV) was responsible for the downward shift of their VBM, leading to the suitable band alignment with the perovskite. Fig. 4C and D show the UPS spectra of the CISe–HTL. The Fermi level (E_F) was found to be −4.23 eV in the high-binding energy regime, which was calculated from the difference between the binding energy cutoff (16.97 eV) and ionization energy of He (21.2 eV) (Fig. 4C) [58]. Additionally, the Fermi edge ($E_{F,edge}$) was found to be 1.19 eV, calculated from the binding energy cutoff in the low-binding energy regime (Fig. 4D) [58]. As the result, the VBM of the CISe–HTL was found to be −5.42 eV by subtracting 1.19 eV from the E_F [58]. Further, since the E_g of the CISe–HTL was 1.3 eV, the conduction band minimum (CBM) was found to be −4.12 eV. Considering the VBM of the perovskite (−5.4 to −5.5 eV), the hole injection from the perovskite to the CISe–HTL would be facilitated owing to the low-hole injection barrier, as described in the inset of Fig. 4D.

Fig. 5A shows the cross-section SEM image of the PSC that employs a 40 nm thick CISe–HTL. Recently, SnO_2 nanoparticles have been

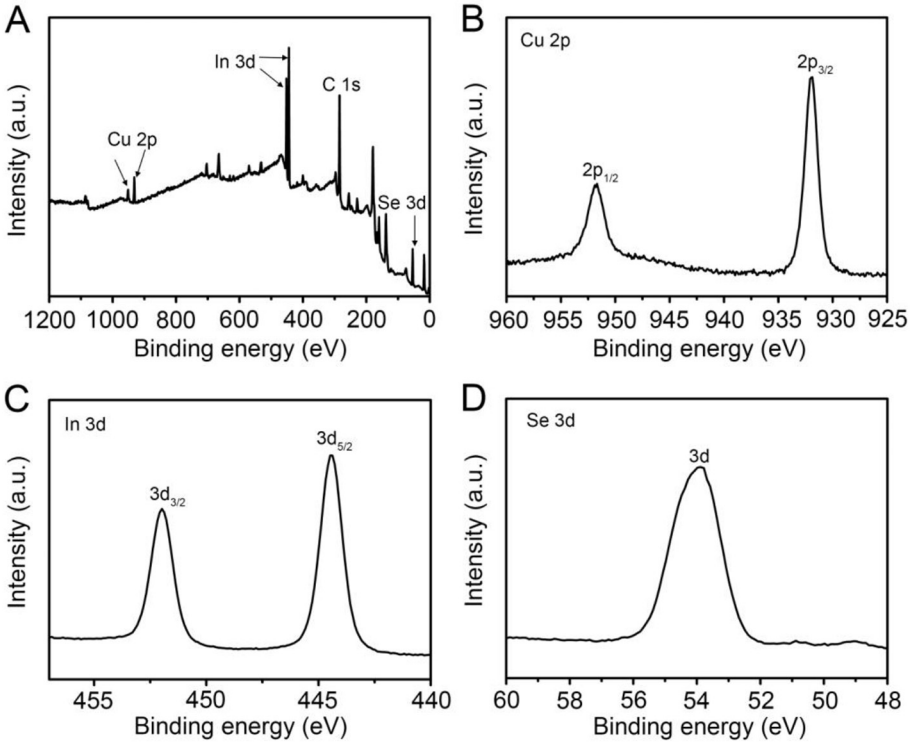

Fig. 3. High-resolution XPS results of the CISe-HTL for (A) overall spectrum, (B) Cu 2p spectrum, (C) In 3d spectrum, and (D) Se 3d spectrum.

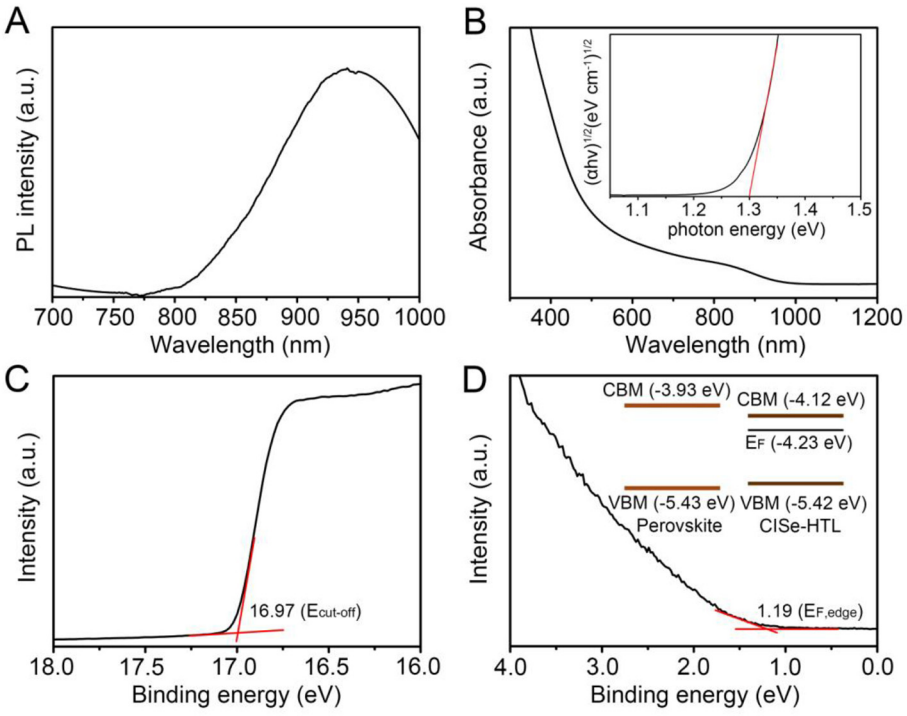

Fig. 4. Characterization of optical properties and electronic structure of the CISe-HTLs. (A) Steady-state PL spectrum of the CISe-HTL. (B) UV–Vis spectrum of the CISe-HTL. The inset graph indicates the Tauc plot of the CISe-HTL. (C and D) High-resolution UPS spectra of the CISe-HTL obtained at the high- and low-binding energy regime, respectively.

considered as a promising material for use in the ETLs in PSCs because they exhibit excellent PCEs (> 20%) [59–61]. The SnO_2–ETLs are thin (~30 nm), smooth, pinhole-free, and highly conductive, and efficiently transfer the electrons from the perovskite. In addition, the fabrication process of the SnO_2–ETLs is simple, and only requires the spin coating of the SnO_2 colloidal solution and the thermal annealing at low temperature (< 150 °C). Therefore, SnO_2–ETLs were employed in our devices. A 500 nm thick perovskite was deposited onto the SnO_2–ETLs using several droplets of ethyl acetate (EA), and was used as an antisolvent to form homogeneous PbI_2–MAI complexes [62]. Following the thermal annealing process at 100 °C, a 40 nm thick CISe–HTL layer was deposited onto the perovskite by spin coating. Finally, Au electrodes were deposited using a thermal evaporator. The energy diagram in Fig. 5B shows the charge transfer from the perovskite to the SnO_2–ETL, CISe–HTL and the electrodes. The device performance was characterized as a function of the thickness of the CISe–HTLs, which ranged from 20 nm to 60 nm. The morphologies and charge transfer behaviors of the CISe–HTLs would be strongly affected by their film

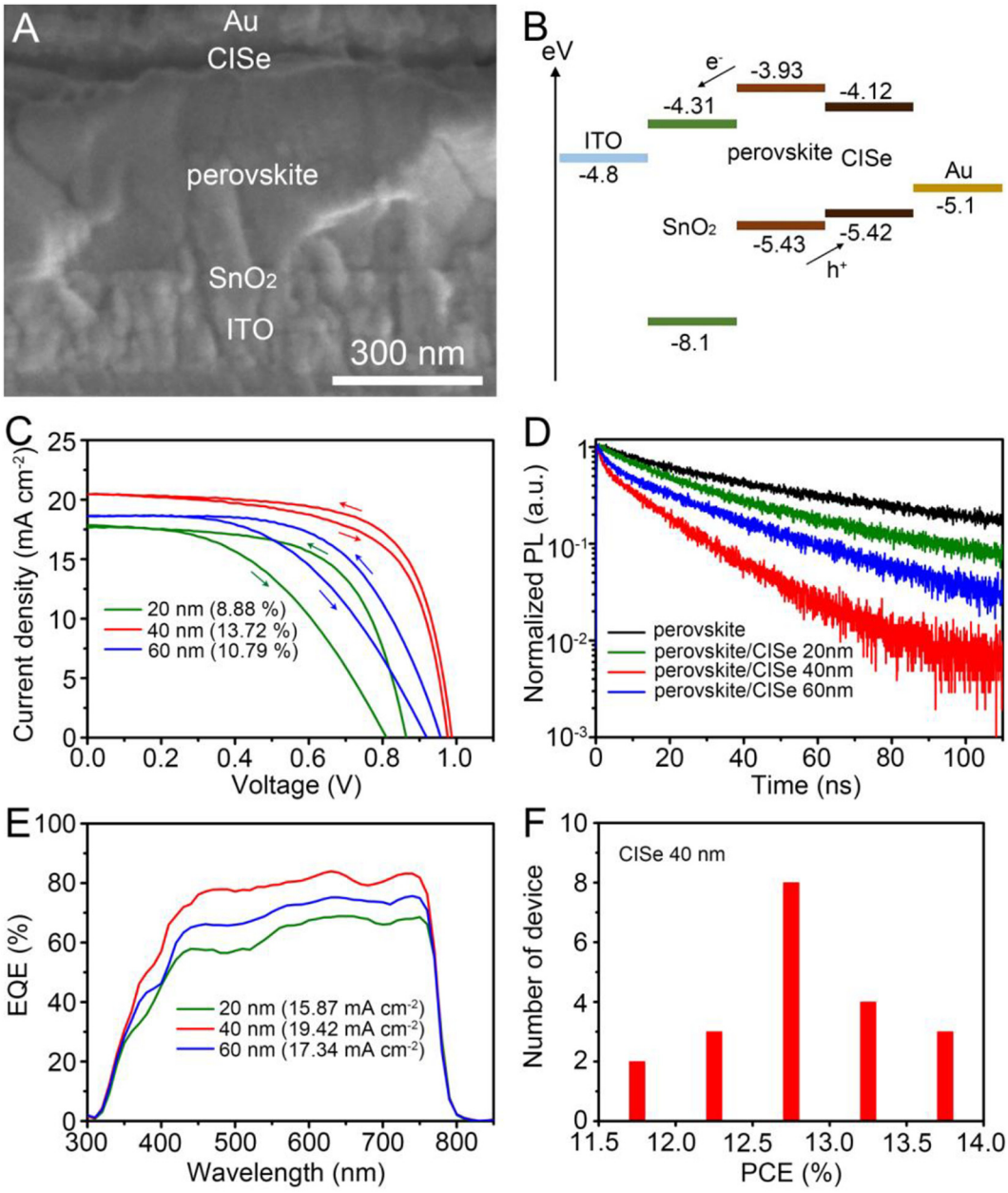

Fig. 5. Characterization of the PSCs employing the CISe-HTLs. (A) Cross-section SEM image of the device. (B) Energy diagram of the device describing the charge transfer from the perovskite to the respective layers. (C) $J-V$ curves of the CISe-devices employing different thickness in the CISe-HTLs (20 nm, 40 nm, and 60 nm). They were obtained under 1 sun condition. (D) TRPL decay curves for the glass/perovskite, glass/perovskite/CISe-20 nm, glass/perovskite/CISe-40 nm, and glass/perovskite/CISe-60 nm. (E) EQE spectra of the CISe-devices employing different thickness in the CISe-HTLs (20 nm, 40 nm, and 60 nm). (F) Histogram of twenty CISe-devices (thickness of HTL = 40 nm).

thicknesses. For the 20 nm thick HTLs, small pinholes were generated, while thick films (40 nm and 60 nm) did contain any pinholes (Fig. S4, ESI†). In spin coating of the CISe–QD solutions, the thickness of HTLs (20 nm, 40 nm, and 60 nm) is controlled by adjusting the concentration of CISe QDs to be 10 mg/mL, 15 mg/mL, and 25 mg/mL, respectively. For the dilute solution (10 mg/mL), the CISe QDs cannot be fully covered on the perovskite due to their low density, in turn, many pinholes are generated certainly. The similar result has been reported in the previous work, demonstrating the generation of small pinholes in the thin film (< 20 nm) during spin coating of a TiO_2–nanocrystal solution (diameter of TiO_2 = 6 nm) [35]. Therefore, the pinhole-free HTLs can be obtained when the film thickness becomes at least 40 nm. For the 60 nm thick HTLs, the transfer path of holes became longer, and accompanied the suppression of the hole transfer by oleylamine ligands at the QD interlayers. It should be noted that the hole transfer in the devices is significantly affected by the tunneling barrier generated within the CISe–HTLs. Since the alkyl chains adhered to the surface of the CISe QDs play a role of the hole transfer barrier, the control of the CISe–HTLs with optimal thickness is significant to attain the efficient hole transfer and pinhole-free morphologies simultaneously [63,64]. In this study, the optimized thickness of the CISe–HTLs was found to be 40 nm. Fig. 5C shows the J–V curves of the devices corresponding to different CISe–HTL thickness (in devices with respective thickness values of 20 nm, 40 nm, and 60 nm). The device with the best performance was the 40 nm–device, which exhibited a V_{oc} of 0.979 V, a fill factor (FF) of 0.685, a current density (J_{sc}) of 20.46 mA cm^{-2}, and yielded an impressive PCE of 13.72% for the backward sweep at a scan delay time of 200 ms. This was the highest value among all the devices that employed

Table 1
Photovoltaic parameters of CISe-devices measured with a standard AM 1.5 G illumination of 100 mW cm^{-2}.[a]

Thickness of CISe-HTLs [nm]	Scan direction	V_{oc} [V]	J_{sc} [mA cm^{-2}]	FF	PCE [%]
20	Backward	0.857 (0.842)	17.84 (16.93)	0.581 (0.530)	8.88 (7.56)
	Forward	0.796	17.67	0.513	7.21
40	Backward	0.979 (0.965)	20.46 (20.32)	0.685 (0.654)	13.72 (12.83)
	Forward	0.967	20.42	0.662	13.07
60	Backward	0.954 (0.935)	18.72 (17.58)	0.604 (0.589)	10.79 (9.68)
	Forward	0.918	18.59	0.523	8.92

[a] The values in brackets are the average values calculated from 20 devices.

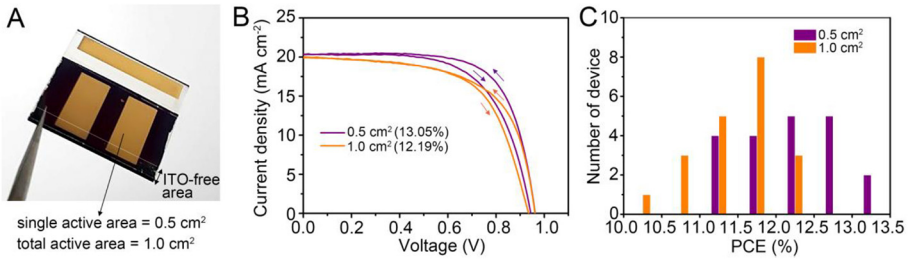

Fig. 6. The characterization of CISe-devices at the large active areas of 0.5 cm^2 and 1.0 cm^2. (A) Photograph of the CISe-device with single active area of 0.5 cm^2. (B) *J-V curves* of the devices measured at the active areas of 0.5 cm^2 and 1.0 cm^2. They were obtained under 1 sun condition. (C) Histogram of twenty CISe-devices for the active areas of 0.5 cm^2 and 1.0 cm^2.

chalcogenide QD–HTLs. In the case of the best performing device, a stabilized PCE of 13.14% was also achieved from a steady state photocurrent density of 17.97 mA cm^{-2} at a maximum power voltage (V_{max}) of 0.731 V (Fig. S5). The PCE of this device was found to be 13.07% for the forward sweep at a scan delay time of 200 ms. The slight hysteresis behavior observed following the backward and forward sweeps was attributed to the charge accumulation at the interface of perovskite/CISe–HTL. The oleylamine ligands linked to the surface of CISe QDs may hinder the reversible transfer of charge carriers, and may thus lead to the charge recombination and the performance degradation of the device. The 20 nm– and 60 nm–devices also exhibited a significant decrease in device performance (PCE = 8.88% and 10.79%, respectively) with more predominant hysteresis owing to the pinholes or the short conductive paths within the HTLs. For the 20 nm thick CISe-HTL, the pinholes in the HTL provide the path of direct contact between the Au electrode and perovskite. Therefore, the charge recombination at their interfaces becomes dominant, which leads to the severe degradation of device performance [65]. The device parameters are listed in Table 1.

The time-resolved PL (TRPL) analysis provides information of the charge transfer behaviors at the interface of perovskite/CISe-HTL. Fig. 5D shows the PL decay curves and the corresponding PL lifetimes in four samples of the glass/perovskite and glass/perovskite/CISe complexes (20–60 nm). These were fitted with the use of a bi-exponential decay function. The fitted parameters for the samples are listed in Table S1 (ESI†). The fast decay corresponds to the quenching of holes between the perovskite and the CISe–HTLs, while the slow decay is attributed to the radiative decay within the perovskite film [66–68]. The average PL lifetimes were found to be 70.67, 38.81, 14.89, and 28.50 ns, for the glass/perovskite, glass/perovskite/CISe (20 nm), glass/perovskite/CISe (40 nm), and glass/perovskite/CISe (60 nm), respectively. Based on the shorter PL lifetime for the glass/perovskite/40 nm–CISe, the hole injection from the perovskite to the CISe–HTL becomes dominant. The faster hole transfer suppresses the charge recombination at the interface of perovskite/CISe–HTL, and improves all the device parameters and the hysteretic behavior. Fig. 5E shows the EQE spectra corresponding to the devices with the thicknesses of 20 nm, 40 nm, and 60 nm. For all the devices, the EQE values were retained from 550 nm to 750 nm, and the spectral peaks were found to be near 640 nm. However, in the case of the 20 nm– and 60 nm–devices, their EQE values dramatically decreased because the charge recombination became dominant either by a) the direct contact of the perovskite and Au electrodes through the pinholes within the thin CISe–HTL, or b) the retardation of the hole transfer process within the thick CISe–HTLs owing to the oleylamine ligands. The integrated J_{sc} values were found to be 15.87 mA cm^{-2}, 19.42 mA cm^{-2}, and 17.34 mA cm^{-2}, for the 20 nm–, 40 nm–, and 60 nm–devices, respectively. These values show excellent agreement with the corresponding J_{sc} values obtained at the J–V curves. The synergetic PL effect of CISe QDs on the generation of extra charge carriers was not observed because the thick perovskite absorbs visible light. The small amount of PL generated by the CISe–HTL at infrared regions cannot contribute to the increase in J_{sc}. We also evaluated the PCEs of twenty independent devices to demonstrate the reproducibility. Since the synthesis of monodispersed CISe QDs is highly reproducible, the similar quality of HTLs was also retained for each device. The average PCE of the 40 nm devices was found to be 12.83% (Fig. 5E).

We further investigated the feasibility of large-area devices employing the CISe-HTLs. Beyond the small active area (0.12 cm^2) of the devices, the device performance at the larger active areas (0.5 cm^2 and 1.0 cm^2) was evaluated. Fig. 6A shows the photograph of the CISe-device (thickness of the CISe-HTL = 40 nm) comprising two active areas of 0.5 cm^2 (total area = 1.0 cm^2). Fig. 6B exhibits the J–V curves of the device for the active areas of 0.5 cm^2 and 1.0 cm^2. Their PCEs were found to be 13.05% and 12.19% for 0.5 cm^2 and 1.0 cm^2, respectively, slightly lower than those measured at the small active area. The slight degradation of the PCEs was mainly attributed to the decrease in the FF. The FF strongly depended on the contact resistance (R_s) raised by the interfacial area of the device. This relationship can be expressed by the following equations [26]:

$$FF = FF'(1 - r) \tag{2}$$

$$r = \frac{R_s}{R'} \tag{3}$$

$$R' = \frac{V_{MP}}{I_{MP}} \tag{4}$$

where FF′ is the fill factor without R_s, r is the normalized R_s, and R′ is the ratio of the voltage (V_{MP}) and photocurrent (I_{MP}) at the maximum point. Therefore, the increasing R_s degraded the FF of the devices, which also led to the distinct hysteresis behavior. The PCEs measured at the forward sweeps were found to be 12.33% and 11.21% for 0.5 cm^2 and 1.0 cm^2, respectively. However, the small PCE deviations raised by the increasing active area are encouraging, suggesting that the CISe QDs are highly suitable for the HTL of the large-area PSCs. Thanks to the thin and uniform deposition of the CISe QDs, the excellent surface

Table 2
Photovoltaic parameters of CISe-devices (active area = 0.5 cm^2 and 1.0 cm^2) measured with a standard AM 1.5 G illumination of 100 mW cm^{-2}.[a]

Active area [cm^2]	Scan direction	V_{oc} [V]	J_{sc} [mA cm^{-2}]	FF	PCE [%]
0.5	Backward	0.962 (0.946)	20.31 (20.18)	0.668 (0.639)	13.05 (12.2)
	Forward	0.946	20.31	0.642	12.33
1.0	Backward	0.957 (0.942)	20.03 (19.89)	0.636 (0.613)	12.19 (11.49)
	Forward	0.935	19.96	0.601	11.21

[a] The values in brackets are the average values calculated from 20 devices.

coverage yielded high reproducibility of the device performance. Fig. 6C exhibits the histogram for the PCEs of twenty independent devices for active areas of 0.5 cm^2 and 1.0 cm^2. The average PCEs were found to be 12.2% and 11.49% for 0.5 cm^2 and 1.0 cm^2, respectively. The device parameters obtained at the active areas of 0.5 cm^2 and 1.0 cm^2 are summarized in Table 2.

Finally, long-term stability tests of the devices were performed for 30 d at RH = 25% and 50% in dark chambers. To compare the stability of the devices based on the CISe–HTL (CISe device) and spiro–HTL (spiro device), the J–V curve of the spiro device was obtained, and yielded a PCE value of 18.13% (Fig. S6, ESI†). At RH = 25%, the CISe and spiro devices showed respective PCE retentions of 89.2% (PCE = 12.16%) and 51.6% (PCE = 9.41%) relative to the initial values after 30 d (Fig. 7A). Since the hydrophobic CISe–HTLs effectively stabilize the perovskite under a moderate humid atmosphere, the device performance can be retained for prolonged periods. Larger differences in the stabilities of the two devices were observed in more humid environments. At RH = 50%, the CISe and spiro devices showed respective PCE retentions of 74.9% (PCE = 10.23%) and 23.5% (PCE = 4.25%) relative to the initial values after 30 d (Fig. 7B). Fig. 7C and D show the conductivity curves of the spiro– and CISe–HTLs at RH = 25% and 50%, respectively. After 30 d, the conductivities of the hygroscopic spiro–HTLs significantly dropped from 2.35×10^{-3} S cm^{-1} to 1.02×10^{-4} S cm^{-1} and to 3.37×10^{-6} S cm^{-1} at RH = 25% and 50%, respectively. However, the conductivity values of the CISe–HTLs slightly decreased from 0.62×10^{-3} S cm^{-1} to 0.37×10^{-3} S cm^{-1} and to 0.12×10^{-3} S cm^{-1} at RH = 25% and 50%, respectively. The lower conductivities of the CISe–HTLs compared to that of a bulk CISe crystal (6–400 S cm^{-1}) can be attributed to the contact resistance between the QDs and the oleylamine ligands which are linked to the CISe QDs [48]. Even though the slow degradation of CISe QDs by oxidation is inevitable, the degradation of the perovskite by moisture was considerably delayed in humid environments (Fig. S7A, ESI†). In addition to the decrease of the conductivity values, the penetrated moisture through the spiro–HTLs dissolves the perovskite and accelerates the degradation of the performance of the device (Fig. S7B, ESI†). The next step in our future plan would be the surface modification of CISe QDs with shorter alkyl chains or inorganic layers to optimize the device performance and stability.

4. Conclusion

In conclusion, monodispersed CISe QDs were used as dual-function HTLs for PSCs. Accordingly, they facilitated the hole transport and protected the perovskite from moisture. They were dispersed in a nonpolar solvent that enabled the deposition of CISe QDs onto the perovskite. The suitable VBM position of the CISe–HTLs with respect to that of the perovskite allowed efficient hole injections. Furthermore, highly conductive CISe–HTLs drove the hole transfer process from the perovskite to Au electrodes. Thereby, an impressive PCE of 13.72% could be achieved, which was well retained for 30 d even at the high RH level of 50%. In contrast, spiro-devices exhibited poor stability in humid environment, even though the initial PCE was high. Therefore, the hydrophobic oleylamine ligands linked to the CISe QDs can effectively suppress the degradation of the perovskite and CISe QDs from

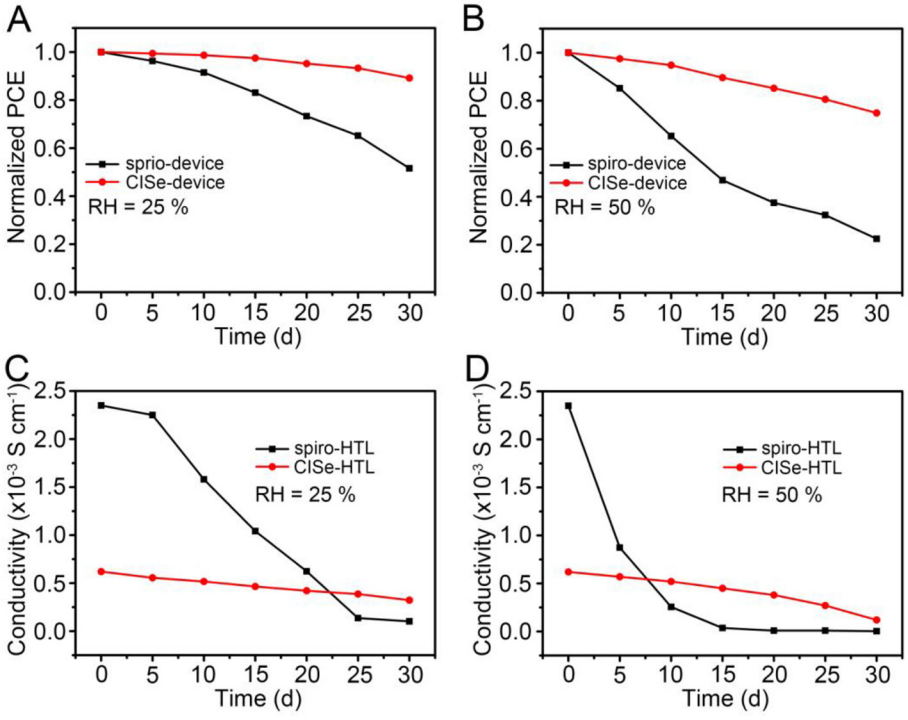

Fig. 7. Long-term stability tests of the CISe- and spiro-devices, and the corresponding HTLs at RH = 25% and 50% for 30 d. (A and B) Normalized PCEs of the devices obtained at RH = 25% and 50% for 30 d, respectively. (C and D) Electrical conductivities of the HTLs obtained at RH = 25% and RH = 50% for 30 d, respectively. All measurements were performed at room temperature.

moisture. Through the surface engineering yielding such hydrophobic QDs, highly stabilized PSCs with excellent device performance would be realized.

Acknowledgements

M. Park acknowledges the financial support by the Basic Science Research Program through the National Research Foundation of Korea (NRF) funded by the Ministry of Science, ICT and Future Planning (NRF-2019R1C1C1005129) in Korea. T. Hyeon acknowledges the financial support by the Research Center Program of the IBS (IBS-R006-D1) in Korea.

Appendix A. Supplementary data

Supplementary data to this article can be found online at https://doi.org/10.1016/j.apsusc.2019.143610.

References

[1] M. Liu, M.B. Johnston, H.J. Snaith, Efficient planar heterojunction perovskite solar cells by vapour deposition, Nature 501 (2013) 395–398.
[2] A. Kojima, K. Teshima, Y. Shirai, T. Miyasaka, Organometal halide perovskite as visible-light sensitizers for photovoltaic cells, J. Am. Chem. Soc. 131 (2009) 6050–6051.
[3] N.-G. Park, M. Grätzel, T. Miyasaka, K. Zhu, K. Emergy, Towards stable and commercially available perovskite solar cells, Nat. Energy 1 (2016) 16152.
[4] National Renewable Energy Laboratory (NREL) Efficiency Chart, www.nrel.gov/pv/assets/pv-efficiency-chart.20190128.pdf, (2019).
[5] N.J. Jeon, J.H. Noh, W.S. Yang, Y.C. Kin, S. Ryu, J. Seo, S.I. Seok, Compositional engineering of perovskite materials for high-performance solar cells, Nature 517 (2015) 476–480.
[6] H. Zhou, Q. Chen, G. Li, S. Luo, T. Song, H. Duan, Z. Hong, J. You, Y. Liu, Y. Yang, Interface engineering of highly efficient perovskite solar cells, Science 345 (2014) 542–546.
[7] G. Yang, C. Wang, H. Lei, X. Zheng, P. Qin, L. Xiong, X. Zhao, Y. Yan, G. Fang, Interface engineering in planar perovskite solar cells: energy level alignment, perovskite morphology control and high performance achievement, J. Mater. Chem. A 5 (2017) 1658–1666.
[8] A. Guerrero, J. You, C. Aranda, Y.S. Kang, G. Garcia-Belmonte, H. Zhou, J. Bisquert, Y. Yang, Interfacial degradation of planar lead halide perovskite solar cells, ACS Nano 10 (2016) 218–224.
[9] S.P. Senanayak, B. Yang, T.H. Thomas, N. Giesbrecht, W. Huang, E. Gann, B. Nair, K. Goedel, S. Guha, X. Moya, R.H. Friend, H. Sirringhaus, Understanding charge transport in lead iodide perovskite thin-film field-effect transistors, Sci. Adv. 3 (2017) e1601935.
[10] F. Li, C. Ma, H. Wang, W. Hu, A.D. Sheikh, T. Wu, Ambipolar solution-processed hybrid perovskite phototransistors, Nat. Commun. 6 (2015) 8238.
[11] S.G.R. Bade, J. Li, X. Shan, Y. Ling, Y. Tian, T. Dilbeck, T. Besara, T. Geske, H. Gao, B. Ma, K. Hanson, T. Siegrist, G. Xu, Z. Yu, Fully printed halide perovskite light-emitting diodes with silver nanowire electrodes, ACS Nano 10 (2016) 1795–1801.
[12] G. Li, Z. Tan, D. Di, M.L. Lai, L. Jiang, J.H. Lim, R.H. Friend, N.C. Greenham, Efficient light-emitting diodes based on nanocrystalline perovskite in a dielectric polymer matrix, Nano Lett. 15 (2015) 2640–2644.
[13] H. Cho, S. Jeong, M. Park, Y. Kim, C. Wolf, C. Lee, J.H. Heo, A. Sadhanala, N.S. Myoung, S. Yoo, S.H. Im, R.H. Friend, T. Lee, Overcoming the electroluminescence efficiency limitations of perovskite light-emitting diodes, Science 350 (2015) 1222–1225.
[14] H. Wang, D.H. Kim, Perovskite-based photodetectors: materials and devices, Chem. Soc. Rev. 46 (2017) 5204–5236.
[15] H. Wang, R. Haroldson, B. Balachandran, A. Zakhidov, S. Sohal, J.Y. Chan, A. Zakhidov, W. Hu, Nanoimprinted perovskite nanograting photodetector with improved efficiency, ACS Nano 10 (2016) 10921–10928.
[16] W. Wei, Y. Zhang, Q. Xu, H. Wei, Y. Fang, Q. Wang, Y. Deng, T. Li, A. Gruverman, L. Cao, J. Huang, Monolithic integration of hybrid perovskite single crystals with heterogeneous substrate for highly sensitive X-ray imaging, Nat. Photonics 11 (2017) 315–322.
[17] C. Gu, J. Lee, Flexible hybrid organic-inorganic perovskite memory, ACS Nano 10 (2016) 5413–5418.
[18] C.C. Stoumpos, C.D. Malliakas, M.G. Kanatzidis, Semiconducting tin and lead iodide perovskites with organic cations: phase transitions, high mobilities, and near-infrared photoluminescent properties, Inorg. Chem. 52 (2013) 9019–9038.
[19] D. Bryant, N. Aristidou, S. Pont, I. Sanzhez-Molina, T. Chotchunangatchaval, S. Wheeler, J.R. Durrant, S.A. Haque, Light and oxygen induced degradation limits the operational stability of methylammonium lead triiodide perovskite solar cells, Energy Environ. Sci. 9 (2016) 1655–1660.
[20] J. Yang, B.D. Siempelkamp, D. Liu, T.L. Kelly, Investigation of $CH_3NH_3PbI_3$ degradation rates and mechanisms in controlled humidity environments using in situ techniques, ACS Nano 9 (2015) 1955–1963.
[21] T. Leijtens, G.E. Eperon, N.K. Noel, S.N. Habisreutinger, A. Petrozza, H.J. Snaith, Stability of metal halide perovskite solar cells, Adv. Energy Mater. 5 (2015) 1500963.
[22] I. Hwang, I. Jeong, J. Lee, M.J. Ko, K. Yong, Enhancing stability of perovskite solar cells to moisture by the facile hydrophobic passivation, ACS Appl. Mater. Interfaces 7 (2015) 17330–17336.
[23] B. Conings, J. Drijkoningen, N. Gauquelin, A. Babayigit, J. D'Haen, L. D'Olieslaeger, A. Ethirajan, J. Verbeeck, J. Manca, E. Mosconi, F.D. Angelis, H. Boyen, Intrinsic thermal instability of methylammonium lead trihalide perovskite, Adv. Energy Mater. 5 (2015) 1500477.
[24] T. Leijtens, T. Giovenzana, S.N. Habisreutinger, J.S. Tinkham, N.K. Noel, B.A. Kamino, G. Sadoughi, A. Sellinger, H.J. Snaith, Hydrophobic organic hole transporters for improved moisture resistance in metal halide perovskite solar cells, ACS Appl. Mater. Interfaces 8 (2016) 5981–5989.
[25] E.J. Juarez-Perez, M.R. Leyden, S. Wang, L.K. Ono, Z. Hawash, Y. Qi, Role of the dopants on the morphological and transport properties of spiro-MeOTAD hole transport layer, Chem. Mater. 28 (2016) 5702–5709.
[26] M. Park, J. Park, I.K. Han, J.Y. Oh, High-performance flexible and air-stable perovskite solar cells with a large active area based on poly(3-hexylthiophene) nanofibrils, J. Mater. Chem. A 4 (2016) 11307–11316.
[27] Z.H. Bakr, Q. Wali, A. Fakharuddin, L. Schmidt-Mende, T.M. Brown, R. Jose, Advances in hole transport materials engineering for stable and efficient perovskite solar cells, Nano Energy 34 (2017) 271–305.
[28] C. Huang, W. Fu, C. Li, Z. Zhang, W. Qiu, M. Shi, P. Heremans, A.K. Jen, H. Chen, Dopant-free hole-transporting material with a C_{3h} symmetrical truxene core for highly efficient perovskite solar cells, J. Am. Chem. Soc. 138 (2016) 2528–2531.
[29] S.N. Habisreutinger, B. Wenger, H.J. Snaith, R.J. Nicholas, Dopant-free planar n-i-p perovskite solar cells with steady-state efficiencies exceeding 18%, ACS Energy Lett. 2 (2017) 622–628.
[30] Y. Liu, Q. Chen, H. Duan, H. Zhou, Y.M. Yang, H. Chen, S. Luo, T. Song, L. Dou, Z. Hong, Y. Yang, A dopant-free organic hole transport material for efficient planar heterojunction perovskite solar cells, J. Mater. Chem. A 3 (2015) 11940–11947.
[31] F. Bella, G. Griffini, J. Correa-Baena, G. Saracco, M. Grätzel, A. Hagfeldt, S. Turri, C. Gerbaldi, Improving efficiency and stability of perovskite solar cells with photocurable fluoropolymers, Science 354 (2016) 203–206.
[32] K. Chu, B.G. Song, H. Yang, D. Kim, C.S. Lee, M. Park, C. Chung, Smart passivation materials with a liquid metal microcapsule as self-healing conductors for sustainable and flexible perovskite solar cells, Adv. Funct. Mater. 8 (2018) 1800110.
[33] Y. Han, S. Meyer, Y. Dkhissi, K. Weber, J.M. Pringle, U. Bach, L. Spiccia, Y. Cheng, Degradation observations of encapsulated planar $CH_3NH_3PbI_3$ perovskite solar cells at high temperatures and humidity, J. Mater. Chem. A 3 (2015) 8139–8147.
[34] J. You, L. Meng, T. Song, T. Guo, Y.M. Yang, W. Chang, Z. Hong, H. Chen, H. Zhou, Q. Chen, Y. Liu, N.D. Marco, Y. Yang, Improved air stability of perovskite solar cells via solution-processed metal oxide transport layers, Nat. Nanotechnol. 11 (2016) 75–81.
[35] U.J. Ryu, S. Jee, J. Park, I.K. Han, J.H. Lee, M. Park, K.M. Choi, Nanocrystalline titanium metal-organic frameworks for highly efficient and flexible perovskite solar cells, ACS Nano 12 (2018) 4968–4975.
[36] S. Chen, S. Chan, Y. Lin, M. Wu, Enhanced power conversion efficiency of perovskite solar cells based on mesoscopic Ag-doped TiO_2 electron transport layer, Appl. Surf. Sci. 469 (2019) 18–26.
[37] I. Jeong, H. Jung, M. Park, J.S. Park, H.J. Son, J. Joo, J. Lee, M.J. Ko, A tailored TiO_2 electron selective layer for high-performance flexible perovskite solar cells via low temperature UV process, Nano Energy 28 (2016) 380–389.
[38] P.S. Chandrasekhar, Y. Seo, Y. Noh, S. Na, Room temperature solution-processed Fe doped NiO_x as a novel hole transport layer for high efficient perovskite solar cells, Appl. Surf. Sci. 481 (2019) 588–596.
[39] S.S. Shin, E.J. Yeom, W.S. Yang, S. Hur, M.G. Kim, J. Im, J. Seo, J.H. Noh, S.I. Seok, Colloidally prepared La-doped $BaSnO_3$ electrodes for efficient, photostable perovskite solar cells, Science 356 (2017) 167–171.
[40] H. Xie, X. Yin, J. Liu, Y. Guo, P. Chen, W. Que, G. Wang, B. Gao, Low temperature solution-derived TiO_2-SnO_2 bilayered electron transport layer for high performance perovskite solar cells, Appl. Surf. Sci. 464 (2019) 700–707.
[41] X. Liu, Z. Wu, Y. Zhang, C. Tsamis, Low temperature Zn-doped TiO_2 as Electron transport layer for 19% efficient planar perovskite solar cells, Appl. Surf. Sci. 471 (2019) 28–35.
[42] J. Choi, S. Song, M.T. Hörantner, H.J. Snaith, T. Park, Well-defined nanostructured, single-crystalline TiO_2 electron transport layer for efficient planar perovskite solar cell, ACS Nano 10 (2016) 6029–6036.
[43] I.M. Hossain, D. Hudry, F. Mathies, T. Abzieher, S. Moghadamzadeh, D. Rueda-Delgado, F. Schackmar, M. Bruns, R. Andriessen, T. Aernouts, F.D. Giacomo, U. Lemmer, B.S. Richards, U.W. Paetzold, A. Hadipour, Scalable processing of low-temperature TiO_2 nanoparticles for high-efficiency perovskite solar cells, ACS Appl. Energy Mater. 2 (2019) 47–58.
[44] X. Yin, P. Chen, M. Que, Y. Xing, W. Que, C. Niu, J. Shao, Highly efficient flexible perovskite solar cells using solution-derived NiO_x hole contacts, ACS Nano 10 (2016) 3630–3636.
[45] H. Zhang, J. Cheng, F. Lin, H. He, J. Mao, K.S. Wong, A.K. Jen, W.C.H. Choy, Pinhole-free and surface-nanostructured NiO_x film by room-temperature solution process for high-performance flexible perovskite solar cells with good stability and reproducibility, ACS Nano 10 (2016) 1503–1511.
[46] Q. Sun, S. Zhou, X. Shi, X. Wang, L. Gao, Z. Li, Y. Hao, Efficiency enhancement of perovskite solar cells via electrospun CuO nanowires as buffer layers, ACS Appl. Mater. Interfaces 10 (2018) 11289–11296.
[47] C. Zuo, L. Ding, Solution processed Cu_2O and CuO as hole transport materials for efficient perovskite solar cells, Small 11 (2015) 5528–5532.
[48] M. Lv, J. Zhu, Y. Huang, Y. Li, Z. Shao, Y. Xu, S. Dai, Colloidal CuInS2 quantum dots

as inorganic hole-transporting material in perovskite solar cells, ACS Appl. Mater. Interfaces 7 (2015) 17482–17488.
[49] Y. Ma, P. Vashishtha, S.B. Shivarudraiah, K. Chen, Y. Liu, J.M. Hodgkiss, J.E. Halpert, A hybrid perovskite solar cell modified with copper indium sulfide nanocrystals to enhance hole transport and moisture stability, Sol. RRL 1 (2017) 1700078.
[50] X. Zhu, B. Cheng, X. Li, J. Zhang, L. Zhang, Enhanced efficiency of perovskite solar cells by PbS quantum dot modification, Appl. Surf. Sci. 487 (2019) 32–40.
[51] J. Kim, J. Yang, J.H. Yu, W. Baek, C. Lee, H.J. Son, T. Hyeon, M.J. Ko, Highly efficient copper-indium-selenide quantum dot solar cells: suppression of carrier recombination by controlled ZnS overlayers, ACS Nano 9 (2015) 11286–11295.
[52] O. Yarema, M. Yarema, V. Wood, Tuning the composition of multicomponent semiconductor nanocrystals: the case of I-II-VI materials, Chem. Mater. 30 (2018) 1446–1461.
[53] S.M.F. Hasan, M.A. Subhan, K. Mannan, The optical and electrical properties of copper indium di-selenide thin films, Opt. Mater. 14 (2000) 329–336.
[54] J. Yang, J. Kim, J.H. Yu, T. Ahn, H. Lee, T. Choi, Y. Kim, J. Joo, M.J. Ko, T. Hyeon, Copper-indium-selenide quantum dot-sensitized solar cells, Phys. Chem. Chem. Phys. 15 (2013) 20517–20525.
[55] Y.N. Liang, K. Yu, Q. Yan, X. Hu, Colloidal $CuInSe_2$ nanocrystals: from gradient stoichiometry toward homogeneous alloyed structure mediated by conducting polymer P3HT, ACS Appl. Mater. Interfaces 5 (2013) 4100–4106.
[56] J.W. Jung, J. Park, I.K. Han, Y. Lee, C. Park, W. Kwon, M. Park, Flexible and highly efficient perovskite solar cells with a large active area incorporating cobalt-doped poly(3-hexylthiophene) for enhanced open-circuit voltage, J. Mater. Chem. A 5 (2017) 12158–12167.
[57] S. Ryu, J.H. Noh, N.J. Jeon, Y.C. Kin, W.S. Yang, J. Seo, S.I. Seok, Voltage output of efficient perovskite solar cells with high open-circuit voltage and fill factor, Energy Environ. Sci. 7 (2014) 2614–2618.
[58] D. Cahen, A. Kahn, Electron energetics at surfaces and interfaces: concepts and experiments, Adv. Mater. 15 (2003) 271–277.
[59] Q. Jiang, L. Zhang, H. Wang, X. Yang, J. Meng, H. Liu, Z. Yin, J. Wu, X. Zhang, J. You, Enhanced electron extraction using SnO_2 for high-efficiency planar-structure $HC(NH_2)_2PbI_3$-based perovskite solar cells, Nat. Energy 2 (2016) 16177.
[60] Q. Jiang, X. Zhang, J. You, SnO_2: a wonderful electron transport layer for perovskite solar cells, Small 14 (2018) 1801154.
[61] E.H. Anaraki, A. Kermanpur, M.T. Mayer, L. Steier, T. Ahmed, S. Turren-Cruz, J. Seo, J. Luo, S.M. Zakeeruddin, W.R. Tress, T. Edvinsson, M. Grätzel, A. Hagfeldt, J. Correa-Baena, Low-temperature Nb-doped SnO_2 electron-selective contact yields over 20% efficiency in planar perovskite solar cells, ACS Energy Lett. 3 (2018) 773–778.
[62] C. Fei, B. Li, R. Zhang, H. Fu, J. Tian, G. Cao, Highly efficient and stable perovskite solar cells based on monolithically grained $CH_3NH_3PbI_3$ film, Adv. Energy Mater. 7 (2017) 1602017.
[63] X. Lv, W. Wei, C. Mu, B. Huang, Y. Dai, Two-dimensional GeSe for high performance thin-film solar cells, J. Mater. Chem. A 6 (2018) 5032–5039.
[64] Y. Liang, Y. Dai, Y. Ma, L. Ju, W. Wei, B. Huang, Novel titanium nitride halide TiNX (X = F, Cl, Br) monolayers: potential materials for highly efficient excitonic solar cells, J. Mater. Chem. A 6 (2018) 2073–2080.
[65] S. Yoon, S.J. Kim, H.S. Kim, J. Park, I.K. Han, J.W. Jung, M. Park, Solution-processed indium oxide electron transporting layers for high-performance and photostable perovskite and organic solar cells, Nanoscale 9 (2017) 16305–16312.
[66] Y. Li, Y. Zhao, Q. Chen, Y.M. Yang, Y. Liu, Z. Hong, Z. Liu, Y. Hsieh, L. Meng, Y. Li, Y. Yang, Multifunctional fullerene derivative for interface engineering in perovskite solar cells, J. Am. Chem. Soc. 137 (2015) 15540–15547.
[67] L. Zuo, Z. Gu, T. Ye, W. Fu, G. Wu, H. Li, H. Chen, Enhanced photovoltaic performance of $CH_3NH_3PbI_3$ perovskite solar cells through interfacial engineering using self-assembling monolayer, J. Am. Chem. Soc. 137 (2015) 2674–2679.
[68] P. Liang, C. Liao, C. Chueh, F. Zuo, S.T. Williams, X. Xin, J. Lin, A.K. Jen, Additive enhanced crystallization of solution-processed perovskite for highly efficient planar-heterojunction solar cells, Adv. Mater. 26 (2014) 3748–3754.